Voronoi-based Interpolants for Fracture Modelling

N. Sukumar and J. E. Bolander

Department of Civil and Environmental Engineering, University of California, Davis, CA 95616. {`nsukumar,jebolander`}`@ucdavis.edu`

Summary. In this paper, we present several applications in solid mechanics that have ties to the Voronoi diagram and the concept of *natural neighbours*. Material structure in metallic alloys and biomaterials are naturally described using the geometric construct known as Voronoi tessellation. For a nodal discretization of a domain in $\mathbf{R}^d$, the corresponding Voronoi diagram defines *natural neighbours*, which determine spatial relationships between nodes and an associated scaling. The use of natural neighbour interpolants within a meshfree Galerkin method (natural element method) for the solution of partial differential equations, the development of polygonal finite elements, and continuum (extended finite element) and lattice approaches to modelling crack propagation are emphasized. These diverse applications demonstrate several advantages of adopting Voronoi grids and natural neighbour interpolants in computer modelling and simulation of physical phenomena.

1 Introduction

The Voronoi tessellation is a fundamental geometrical construct that has been widely used to describe the material structure in polycrystalline alloys, cellular foams, geomaterials, trabecular bone, and other materials that exhibit cell-like features. For such applications, numerical modelling and simulation on Voronoi meshes is a natural choice. Finite element analyses can be based on the Delaunay/Voronoi dual tessellations for both defining the computational mesh and approximating the field quantity within each element. Interpolants that are based on the Voronoi diagram are of more recent origin, with Sibson's interpolant [48] being the first Voronoi-based interpolation scheme. Over the past decade, Voronoi-based interpolants have been adopted in diverse applications in mechanics—in meshfree Galerkin methods (natural element method) [11, 13, 14, 49, 54, 55], towards the conception of a finite volume or equivalently a finite difference discretization on Voronoi meshes [41, 50], in the development of polygonal and polyhedral finite elements [31, 32, 56], and to model crack propagation using irregular lattice networks [7, 9, 10].

The remainder of this paper is organized as follows. In the next section, we provide a short introduction to natural neighbour interpolants and then focus on two recent applications of Voronoi interpolants in fracture mechanics. Section 2.3 describes the construction of polygonal interpolants using natural neighbour basis functions and presents applications of barycentric finite elements for mesh-independent crack growth modelling. In Section 3, Delaunay/Voronoi-based lattice models are used to simulate cracking in softening materials. Finally, a few concluding remarks are given in Section 4.

2 Voronoi Diagram and Natural Neighbour Interpolants

Given a set of nodes $\mathbf{N} = \{n_1, n_2, \ldots, n_M\}$ in $\mathbf{R}^d$, the Voronoi diagram $V(\mathbf{N})$ of the set $\mathbf{N}$ is a subdivision of the domain into regions V_i, such that any point in V_i is closer to node n_i than to any other node $n_j \in \mathbf{N}$ $(j \neq i)$. The first-order Voronoi cell, V_i, within the convex hull is a convex polyhedron in $\mathbf{R}^d$:

$$V_i = \{\mathbf{x} \in \mathbf{R}^d \,:\, d(\mathbf{x}, \mathbf{x}_i) < d(\mathbf{x}, \mathbf{x}_j) \,\forall j \neq i\}, \tag{1}$$

where $d(\cdot, \cdot)$ is the Euclidean distance.

The dual of the Voronoi diagram, the Delaunay tessellation, is constructed by connecting nodes that have a common $(d{-}1)$-dimensional Voronoi facet. In Fig. 1, the Voronoi diagram and the Delaunay triangulation are shown for a set of seven nodes. Delaunay triangles satisfy the *empty circumcircle criterion*— if T is any Delaunay triangle of the nodal set $\mathbf{N}$, then the circumcircle of T contains no other nodes of $\mathbf{N}$ (see Fig. 1a).

Consider now the introduction of a point p with coordinates $\mathbf{x} \in \mathbf{R}^2$ into the domain Ω (Fig. 1b). The Voronoi diagram V or equivalently the Delaunay triangulation DT for the M nodes and the point p is constructed. Now, if the Voronoi cell for p and n_i have a common facet, then the node n_i is said to be a *natural neighbour* of the point p [48]. The Voronoi cells for the point p and its natural neighbours are shown in Fig. 1b.

2.1 Sibson interpolant

The natural neighbour (Sibson) interpolant was introduced by Sibson [48]. The second-order Voronoi diagram of the set of nodes $\mathbf{N}$ is a subdivision of the plane into cells $V_{i,j}$, such that $V_{i,j}$ is the locus of all points that have n_i as the nearest neighbour, and n_j as the second nearest neighbour. The second-order Voronoi cell $V_{i,j}$ $(i \neq j)$ is defined as [48]

$$V_{i,j} = \{\mathbf{x} \in \mathbf{R}^2 \,:\, d(\mathbf{x}, \mathbf{x}_i) < d(\mathbf{x}, \mathbf{x}_j) < d(\mathbf{x}, \mathbf{x}_k) \,\forall k \neq i, j\}. \tag{2}$$

Consider Fig. 2a, where a point p with coordinate $\mathbf{x}$ is inserted into a tessellation. The natural neighbour shape function of p with respect to a
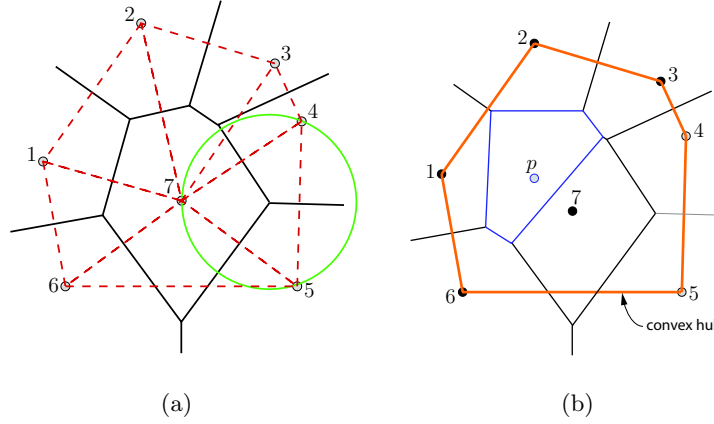
Fig. 1. Voronoi diagram and natural neighbours [50]. (a) Voronoi cells and Delaunay triangulation; and (b) natural neighbours (filled circles) of p.

natural neighbour i is defined as the ratio of the area of the second-order Voronoi cell (A_i) to the total area of the first-order Voronoi cell of p (A):

$$\phi_i(\mathbf{x}) = \frac{A_i(\mathbf{x})}{A(\mathbf{x})}, \quad A(\mathbf{x}) = \sum_{j=1}^{n} A_j(\mathbf{x}), \tag{3}$$

where $n = 5$ for the point p in Fig. 2a. Sibson shape functions are non-negative, interpolate, form a partition of unity, and satisfy the local coordinate property (linear precision) [48]. Stemming from the work of Braun and Sambridge [11] who proposed the *natural element method*, the Sibson interpolant has been widely used as an interpolating function in Galerkin meshfree methods. Survey articles and monographs on meshfree methods are available in the literature [1, 6, 24, 36, 37, 57]. Farin [21] developed a C^1 natural neighbour interpolant, whereas Hiyoshi and Sugihara [28] proposed a general prescription for higher order continuous Voronoi interpolants. Farin's interpolant has been used to solve fourth-order partial differential equations [53]. Cueto *et al.* [13] used the concept of α-shapes [19, 20] to describe nonconvex boundaries within the natural element method. Boissonnat and Flötotto [8] extended the Sibson interpolant to smooth approximations on a surface $((d\text{-}1)$-manifold in $\mathbf{R}^d)$.

2.2 Laplace interpolant

The Laplace interpolant was first proposed by Christ *et al.* [12], and subsequently rediscovered by Belikov *et al.* [4] and Hiyoshi and Sugihara [27]. In $\mathbf{R}^2$, the Laplace shape functions are defined as [12]

$$\phi_i(\mathbf{x}) = \frac{\alpha_i(\mathbf{x})}{\sum\limits_{j=1}^{n} \alpha_j(\mathbf{x})}, \quad \alpha_j(\mathbf{x}) = \frac{s_j(\mathbf{x})}{h_j(\mathbf{x})}, \tag{4}$$

where $\alpha_i(\mathbf{x})$ is the Laplace weight function, $s_i(\mathbf{x})$ is the length of the Voronoi edge associated with p and node i, and $h_i(\mathbf{x})$ is the Euclidean distance between p and node i (see Fig. 2b).

(a)   (b)
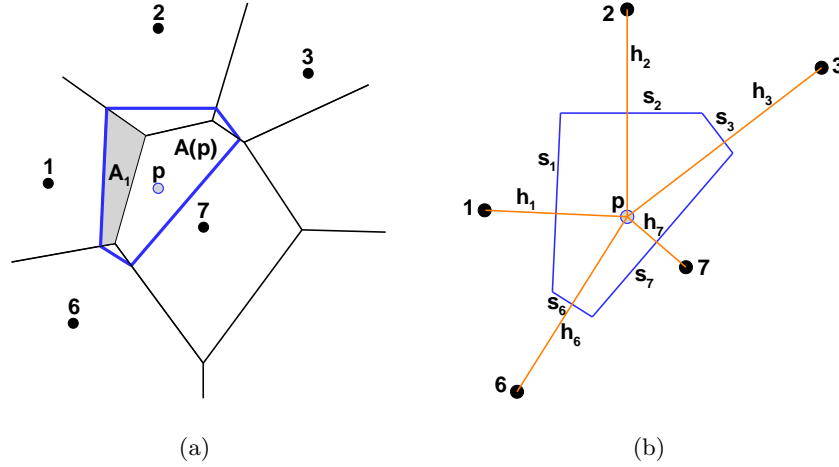
Fig. 2. Natural neighbour-based interpolants [50]. (a) Sibson interpolant; and (b) Laplace interpolant.

Sukumar *et al.* [55] adopted the Laplace interpolant in a Galerkin method for elasticity. An overview of the applications of natural neighbour Galerkin methods in solid and fluid mechanics is presented in Reference [14].

2.3 Planar Polygonal Meshes

Rational finite element basis functions on convex polygons were introduced by Wachspress [63], and in recent years there has been growing interest in the construction of barycentric coordinates on irregular polygons and polyhedra. Many new contributions on barycentric polygonal interpolation have been realized in geometry modelling and graphics, and in finite element methods [17, 22, 23, 29, 38–40, 51, 52, 56]. Barycentric coordinates are non-negative, form a partition of unity, have linear precision, and are linear on element edges. This makes them a suitable candidate for use as a basis in finite element methods. In Reference [56], the Laplace interpolant [12] is used to construct conforming approximations on polygons. This approach is elaborated below.

An interpolation scheme for a scalar-valued function $u(\mathbf{x}) : \Omega \to \mathbf{R}$ is:

$$u^h(\mathbf{x}) = \sum_{i=1}^{n} \phi_i(\mathbf{x}) u_i, \tag{5}$$

where u_i are the unknowns at the n neighbours of point p, and $\{\phi_i\}_{i=1}^{n}$ are the polygonal basis functions. For convergence in linear elasticity, the desirable properties of shape functions are: non-negativity, interpolation, partition of unity, and linear completeness:

$$0 \le \phi_i(\mathbf{x}) \le 1, \quad \phi_i(\mathbf{x}_j) = \delta_{ij}, \quad \sum_{i=1}^{n} \phi_i(\mathbf{x}) = 1, \quad \sum_{i=1}^{n} \phi_i(\boldsymbol{\xi}) \mathbf{x}_i = \mathbf{x}, \tag{6}$$

where $\mathbf{x} = \boldsymbol{\Phi}(\boldsymbol{\xi})$ is the isoparametric mapping, and the shape functions $\phi_i(\boldsymbol{\xi})$ are defined in a canonical element (see Fig. 5).

Given a set of nodes in the plane, the Laplace shape function at a point p within the convex hull is determined using the Voronoi diagram of the nodal set and p. Following the description in Section 2.2, if p lies within the circumcircle of a Delaunay triangle T, the nodes that define T are *natural neighbours* of p [48]. Referring to Fig. 3 and Eq. (4), the shape functions are written as

$$\phi_i(\boldsymbol{\xi}) = \frac{\alpha_i(\boldsymbol{\xi})}{\displaystyle\sum_{j=1}^{n} \alpha_j(\boldsymbol{\xi})}, \quad \alpha_j(\boldsymbol{\xi}) = \frac{s_j(\boldsymbol{\xi})}{h_j(\boldsymbol{\xi})}, \tag{7}$$

where $h_i(\boldsymbol{\xi}) = \|\boldsymbol{\xi} - \boldsymbol{\xi}_i\|_2$ and $s_i(\boldsymbol{\xi})$ is the length of the Voronoi edge. Note that when $\boldsymbol{\xi} \to \boldsymbol{\xi}_i$, the distance $h_i \to 0$, but a limiting argument leads to the result: $\phi_i \to 1$, $\phi_j \to 0$ $(j \ne i)$ [55]. Sibson shape functions are smooth everywhere except at the nodes where they are $C^0(\Omega)$, whereas Laplace shape functions are $C^0(\Omega)$ on the boundary of their support [55] (see Fig. 4). Both the Sibson and Laplace shape functions satisfy all the properties indicated in Eq. (6).

In a simplex-partition of a regular polygon, all triangles have a common center and the nodes all lie on the same circumcircle. For all the polygons shown in Fig. 5, the vertex-nodes lie on the same circumcircle, and hence all the nodes of a polygon are the *natural neighbours* for any point in Ω_0. Since $\phi_i \equiv \phi_i(\boldsymbol{\xi})$ is piece-wise linear on the boundary $\partial \Omega_0$, we use the isoparametric mapping, $\mathbf{x} = \boldsymbol{\Phi}(\boldsymbol{\xi})$, given in Eq. (6), to obtain the shape functions and its gradient on arbitrary convex polygons in the physical space. In Fig. 6, the Laplace basis function $\phi_2(\mathbf{x})$ is plotted on a Voronoi mesh consisting of polygonal elements. We point out that on circumscribable polygons, Wachspress [63], Laplace [12], and discrete harmonic weights [44] are identical. The equivalence between Laplace shape functions and discrete harmonic weights is shown in Reference [52].

Within a Galerkin method, the weak form integrals are numerically computed. Numerical integration is performed by sub-dividing the canonical element into n triangles and then numerical quadrature is performed on each
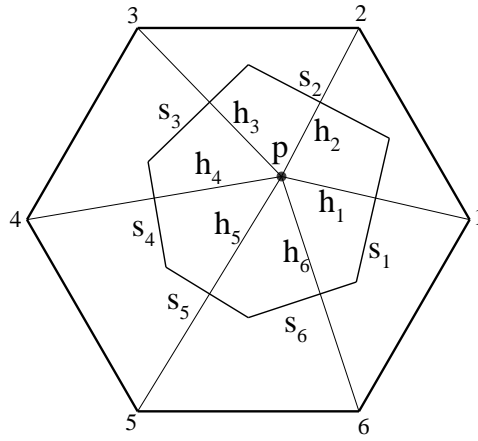
Fig. 3. Laplace shape function.

(a)   (b)
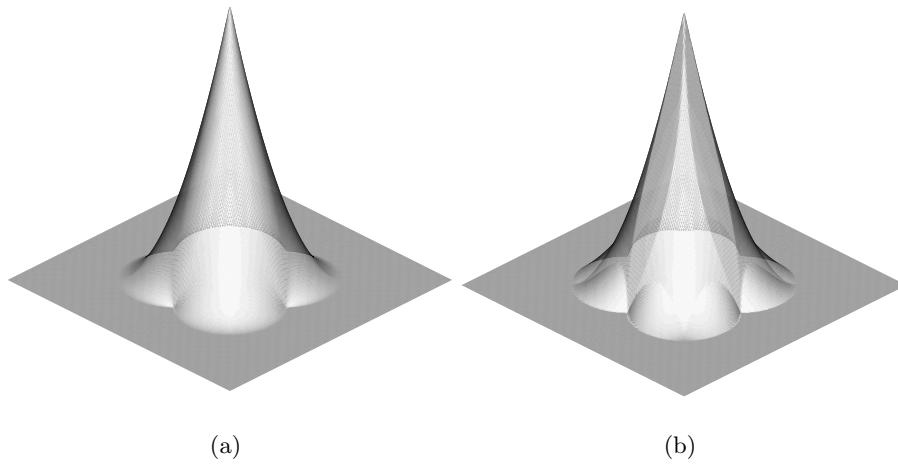
Fig. 4. Plots depicting the support and smoothness of natural-neighbour basis functions [55]. (a) Sibson; and (b) Laplace.

triangle. The above approach of constructing shape functions is a generalization of finite elements to convex n-gons of arbitrary order. For further details on the convergence of the method and its numerical implementation, we point the reader to Reference [56].
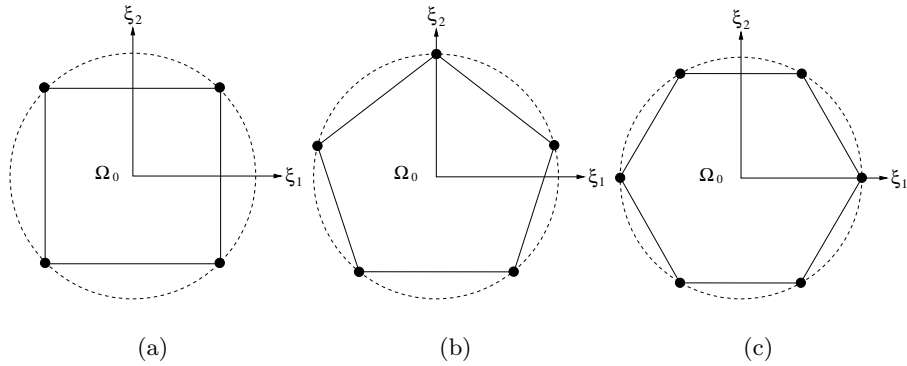
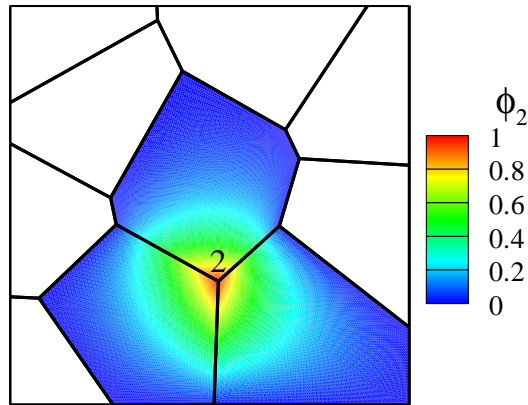**Fig. 5.** Canonical elements in the plane [56].

Fig. 6. Polygonal (Laplace) basis function.

2.4 Quadtree Meshes

Hierarchical grids have a tree-structure [45], which may be represented via a directed graph. In two-dimensions, recursive decomposition of a square leads to a quadtree (Fig. 7). In a quadtree, the domain is enclosed by unit squares (root) that are sub-divided into four equal elements (cells) which are the children of the root. This process can be repeated several times on each of the children until a stopping criterion is met. The level of a cell is the number of refinements needed to obtain that cell; the root is at level zero. In the data
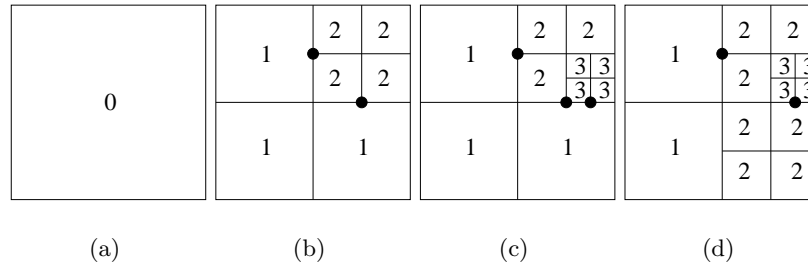
Fig. 7. Quadtree. (a) level 0; (b) levels 0–2; (c) levels 0–3; and (d) levels 0–3 (2:1 rule).

structure, for each cell, we store its connectivity, refinement level, a pointer to its parent, and a pointer to its children.

In Fig. 7, different levels in a quadtree data structure are shown, and the *hanging nodes* are indicated by filled circles. The presence of *hanging nodes* leads to nonconformity across the interface in finite element methods. Hence, it has been the practice with finite elements to minimize the number of hanging nodes across cell interfaces—a constraint (2:1 rule) is imposed such that two adjacent cells can at most differ by one level. Furthermore, Lagrange multipliers, Nitsche's method, or use of multipoint constraints are typically used in finite element methods to address the issue of nonconformity, which complicates the algorithm. In recent years, directly constructing conforming approximations on quadtree meshes has been actively pursued [33–35, 58].

In References [58, 59], conforming approximations are obtained on any quadtree mesh by suitably adapting the construction of conforming polygonal interpolants, which is described in Section 2.3. In Fig. 8a, an isoparametric map from the pentagon in Fig. 5c to element A is shown. From Fig. 8b, we see that the shape function ϕ_a is continuous, and linear behaviour along 1–a and a–2 is realized.

As an illustrative adaptive simulation, consider the following Poisson problem:

$$\nabla^2 u = f \quad \text{in } \Omega = (0,1)^2, \tag{8a}$$

$$u = 0 \quad \text{on } \partial\Omega, \tag{8b}$$

where the source f is chosen so that $u(\mathbf{x}) = x_1{}^{10} x_2{}^{10}(1 - x_1)(1 - x_2)$ is the exact solution. In Fig. 9, the initial mesh and a few refinements are shown. The solution u^h (Fig. 9d) on mesh 9c (928 elements) captures the sharp gradients near $(1, 1)$. The relative L^2 error norm was $O(10^{-10})$ for the patch test on the mesh shown in Fig. 9c.
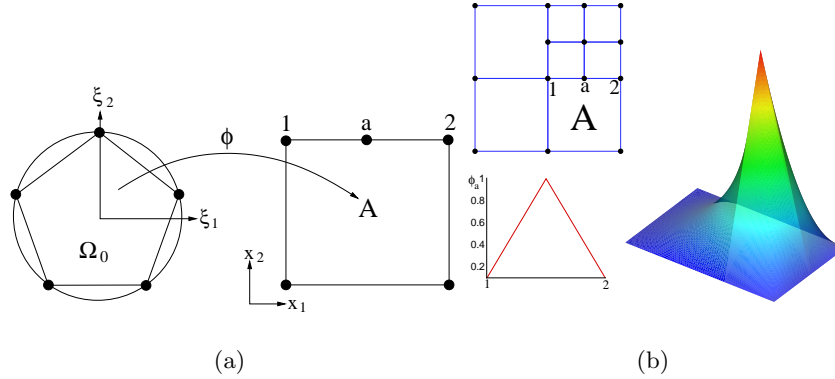
Fig. 8. Shape function ϕ_a on a quadtree mesh [58]. (a) mapping; (b) C^0 conforming.

2.5 Crack Propagation on Polygonal and Quadtree meshes

In finite element analyses, cracks and discontinuities are often explicitly represented via the mesh (i.e., cracks form along the boundaries between elements). For such approaches, mesh regeneration is necessary to follow arbitrary crack trajectories. To accurately reproduce the singular stress fields according to linear elastic fracture mechanics, refined meshes are also needed in the vicinity of the crack tip. An alternative approach that has gained prominence in recent years is mesh-independent modelling of cracks. This is achieved by enriching the displacement approximation by a discontinuous function using the framework of partition of unity [2]. Hence, the mesh no longer needs to conform to the crack geometry and, furthermore, no remeshing is needed in crack propagation simulations. This approach, which is referred to as the extended finite element method (X-FEM), was introduced for triangular and quadrilateral elements in Moës *et al.* [42]. In Reference [60], the X-FEM was extended to polygonal and quadtree meshes.

The enriched displacement approximation for crack modelling in the X-FEM is [42]:

$$\mathbf{u}^h(\mathbf{x}) = \sum_{i \in I} \phi_i(\mathbf{x})\mathbf{u}_i + \sum_{j \in J} \phi_j(\mathbf{x})H(\mathbf{x})\mathbf{a}_j + \sum_{k \in K} \phi_k(\mathbf{x}) \sum_{\alpha=1}^{4} \psi_\alpha(\mathbf{x})\mathbf{b}_{k\alpha}, \quad (9)$$

where $\phi_i(\mathbf{x})$ is the polygonal basis function of node i; $\mathbf{u}_i$ are the classical degrees of freedom associated with node i; $\mathbf{a}_j$ are the enriched degrees of freedom associated with node j and the Heaviside function $H(\mathbf{x})$ (discontinuous across the crack interior); and $\mathbf{b}_{k\alpha}$ are the enriched degrees of freedom associated with node k and the near-tip enrichment functions $\psi_\alpha(\mathbf{x})$, which are defined as [5]

(a)   (b)

(c)   (d)
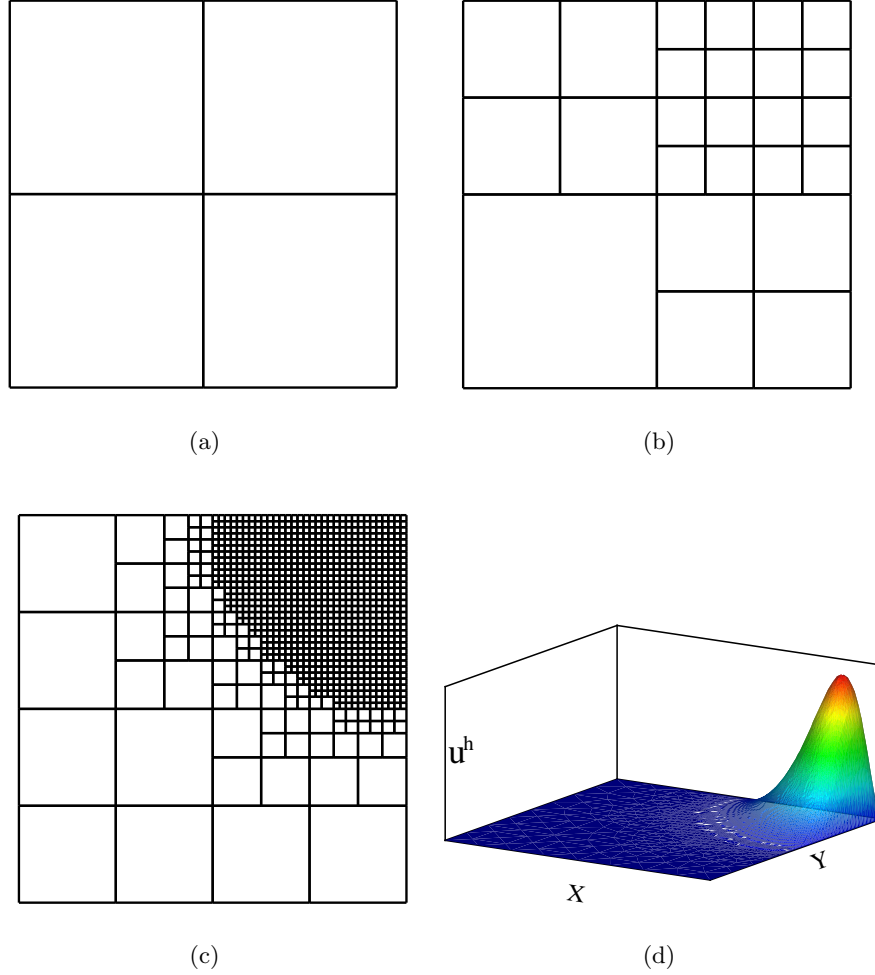
Fig. 9. Quadtree mesh refinements for steps 0,2,5 in (a)–(c); and (d) u^h (step 5).

$$\{\psi_\alpha(\mathbf{x}),\ \alpha=1\text{–}4\} = \left\{\sqrt{r}\sin\frac{\theta}{2}, \sqrt{r}\cos\frac{\theta}{2}, \sqrt{r}\sin\frac{\theta}{2}\sin\theta, \sqrt{r}\cos\frac{\theta}{2}\sin\theta\right\},\ (10)$$

where r and θ are local crack-tip polar coordinates of point $\mathbf{x}$. The index set I consists of all nodes in the mesh, the set K consists of nodes that contain the crack tip within their basis function support closure, and J is the set of nodes whose basis function supports are cut by the crack interior and do not belong to set K. A standard Galerkin weak form of the equations of linear elasticity is used to obtain the discrete equations. Further details on the X-

FEM and its implementation on polygonal and quadtree meshes can be found in Reference [60].

In what follows, quasi-static crack growth simulation on polygonal and quadtree meshes are presented. The crack length increment in each step is equal to twice the length of the element that contains the crack tip, and the kink angle is obtained using the maximum circumferential stress criterion.

Double cantilever beam

A double cantilever beam with a crack lying slightly off the mid-plane is considered. The right end is fixed and unit point loads are applied at the top and bottom of the left end. This problem was solved on a rectangular mesh using the X-FEM in Reference [30].

The beam dimension is 4×1 and the initial crack length is 2 (Fig. 10). The polygonal mesh consists of 500 elements and 1002 nodes. The quadtree mesh has 301 elements and 359 nodes and the level of refinement is 4 in the vicinity of the crack tip. The crack growth simulations are depicted in Figs. 11 and 12 for the polygonal and quadtree meshes, respectively. The quadtree refinement around the crack tip can be seen in the plots presented in Fig. 12. The crack trajectories from the polygonal and quadtree meshes are in qualitative agreement with each other.
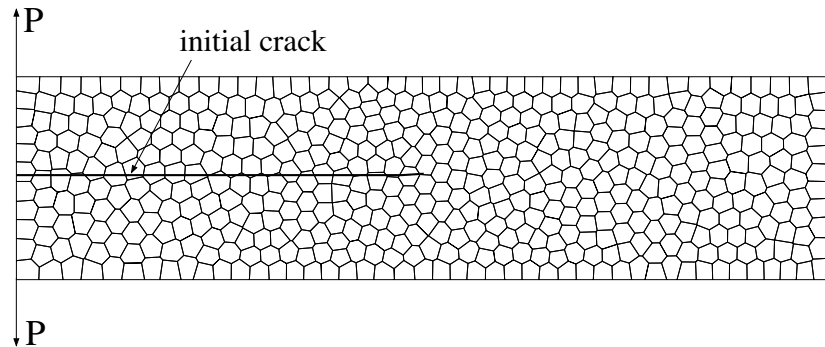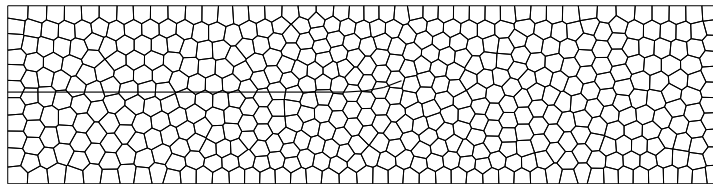

Fig. 10. Pre-cracked double cantilever beam specimen.

Microcrack growth under uniaxial tension

Crack growth of a microstructurally small crack in a rectangular plate under uniaxial tension in the x_2-direction is simulated [60]. The plate dimensions are $L \times L \equiv 10 \times 10$, the angle of the crack with the x_1-axis is 30° and the crack length $a = 0.1$. Since $a/L = 0.01$, use of a quadtree mesh is beneficial to capture the initial crack geometry and to facilitate crack growth simulations.
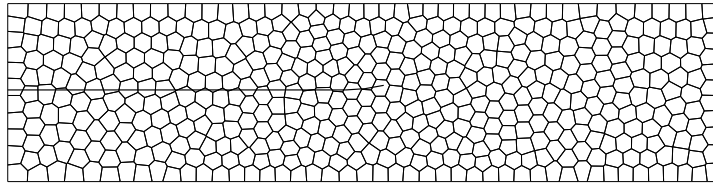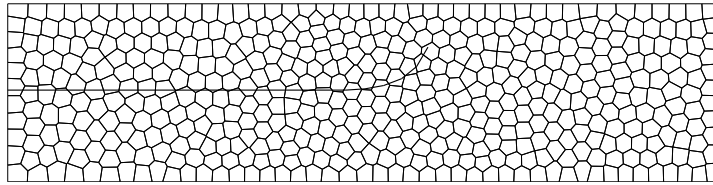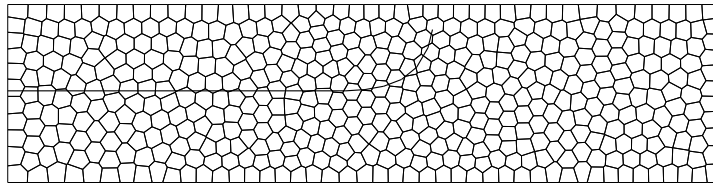
(a)

(b)
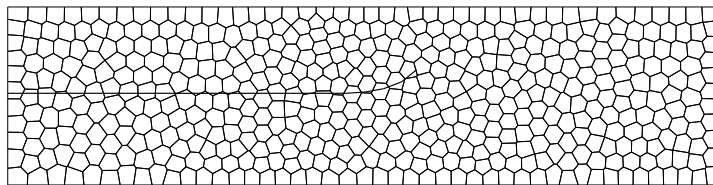
(c)

(d)

(e)

Fig. 11. Crack growth in double cantilever beam specimen. (a)-(e) Steps 2–6 on a polygonal mesh).

(a)

(b)

(c)

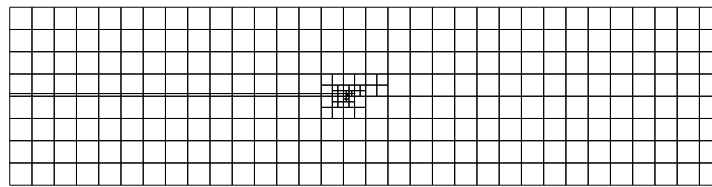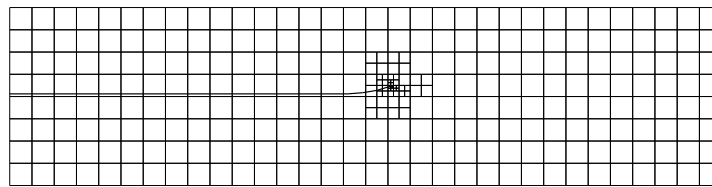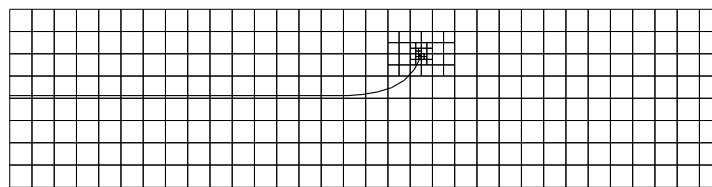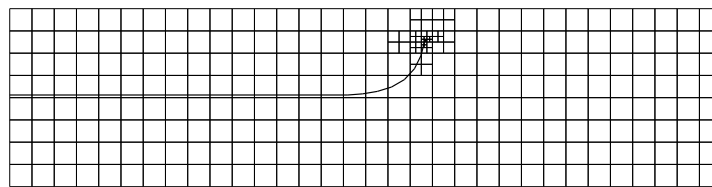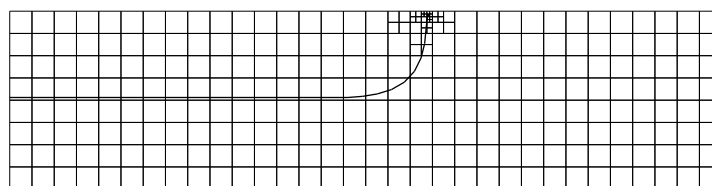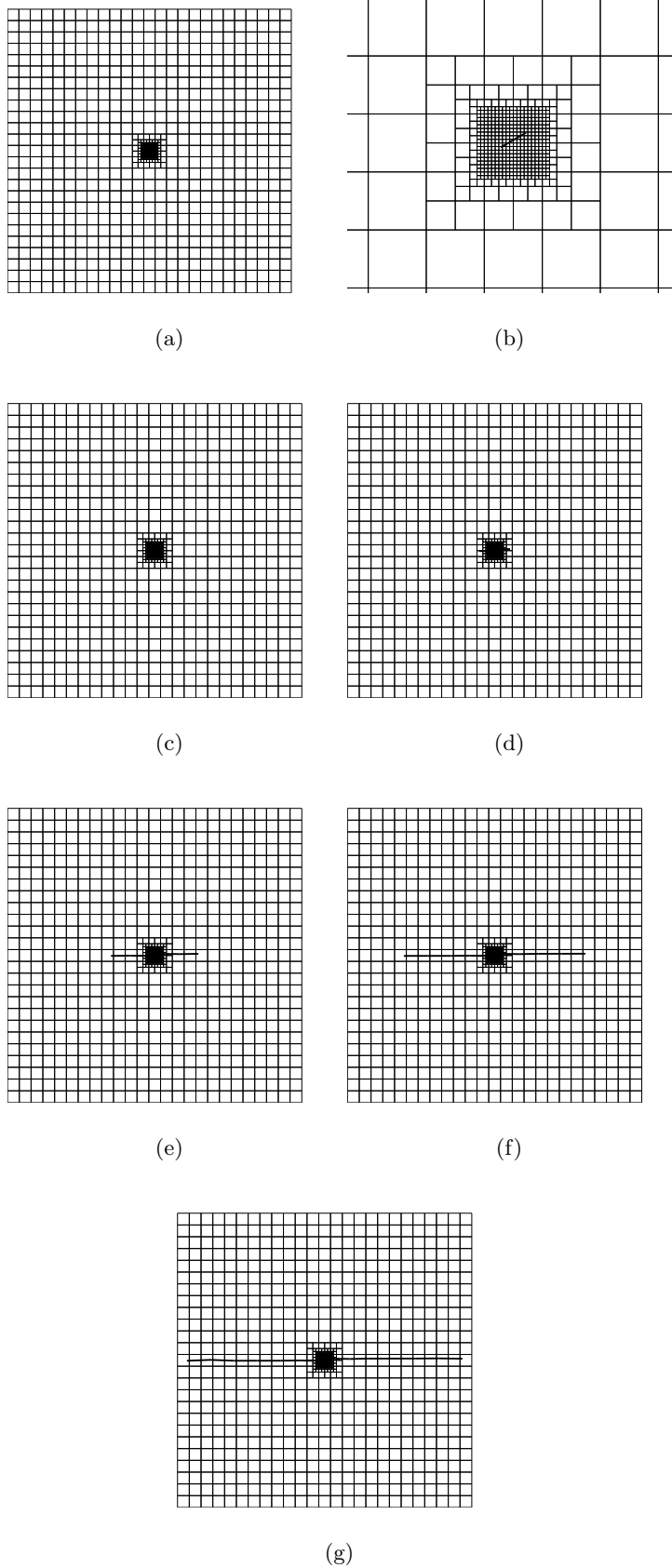

(d)

(e)

Fig. 12. Crack growth in double cantilever beam specimen. (a)-(e) Steps 2–6 on a quadtree mesh).

(a)   (b)

(c)   (d)

(e)   (f)

(g)

Fig. 13. Crack propagation of a microcrack on a quadtree mesh.

The quadtree mesh (1108 elements and 1205 nodes) is shown in Fig. 13a; an enlarged view of the crack region is plotted in Fig. 13b. Since the plate is under pure mode I loading, crack advance should take place along the x_1-direction. The crack paths are illustrated in Figs. 13c–13f, and the final trajectory is along the x_1-direction, which is in agreement with theory.

3 Irregular Lattice Models

Lattice models are composed of simple, one-dimensional elements interconnected on either a regular or irregular array of nodal points. Although basic in their formulations, such models have been useful in understanding complicated aspects of material behaviour, including fracture [25,26,47,61]. By virtue of lattice site symmetry, regular lattices can represent uniform straining of homogeneous media [46]. Lattices constructed on irregularly positioned nodes generally do not satisfy this fundamental requirement, but rather exhibit artificial heterogeneity during straining. For irregular lattice models based on natural neighbour concepts, however, elastically uniform representations of homogeneous media are obtained. The topology of the lattice is determined by the Delaunay tessellation of the lattice nodes, whereas the element stiffness properties scale according to the dual Voronoi tessellation [7,9,10].

This section discusses basic capabilities of irregular lattice models when simulating fracture of quasi-brittle materials. One primary justification for these models is the lattice-like discontinuity of materials at fine scales. However, this section considers modelling at coarser scales for which the material can be regarded as a continuum. Attention is given to fracture in statistically homogeneous materials, i.e., heterogeneity is not explicitly modeled, but rather its effects are simulated via a crack band representation of fracture [3]. One end goal of this work is the development of Delaunay/Voronoi lattice models of fracture of multiphase composites [65]. The confinement-shear lattice (CSL) models of Cusatis *et al.* [15,16] are notable contributions toward this objective.

3.1 Model discretization and formulation

Domain discretization

The lattice model topology and properties are defined by the Delaunay/Voronoi dual tessellation of a set of nodal points (Fig. 14). The discretization process involves the following steps:

- Lattice nodes are inserted in the domain using a process of Random Sequential Addition (RSA) [64]. A minimum allowable distance is maintained between nodes, so that the domain eventually becomes saturated with nodal points. The minimum allowable distance can be a function of

(a)   (b)

(c)
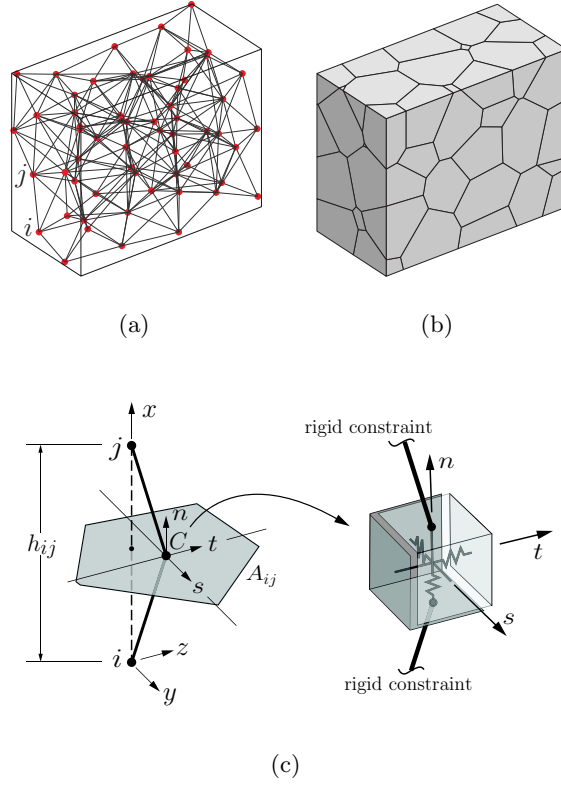
Fig. 14. Domain discretization. (a) Delaunay tessellation of nodal point set; (b) dual Voronoi tessellation; and (c) lattice element.

the spatial coordinates, enabling gradations of nodal point density. Since trial points are rejected with increasing frequency as the domain becomes saturated with nodes, a partitioned domain search is used to accelerate this computationally expensive process [66];

- Domain boundaries are constructed by associating a set of auxiliary points with each lattice node [9, 66]. For each lattice node in a convex domain with M planar surfaces, a corresponding auxiliary point is placed outside the domain for each of the M surfaces. The positioning of the auxiliary points is illustrated in Fig. 15a for two nodes inside a planar domain with $M = 5$. As the number of nodal points increases, the relative proportion of active auxiliary points diminishes. This approach for defining domain boundaries extends naturally to three dimensions (Fig. 15b).
- Voronoi tessellation of the entire point set [43], including auxiliary points that are actively associated with domain boundary construction. The dual

Delaunay tessellation defines the lattice element connectivity between the nodal points (Fig. 14a). Basic non-convex features are discretized by strategically introducing nodes and auxiliary points, prior to the random filling process.
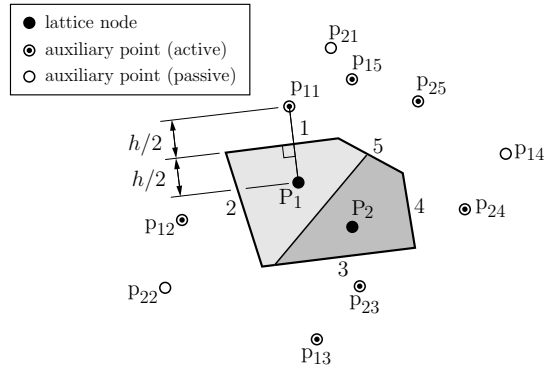
(a)
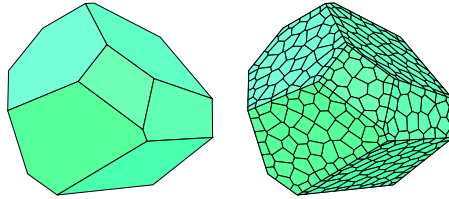
(b)

Fig. 15. (a) Domain boundary definition using auxiliary points; and (b) Voronoi subdivision of a three-dimensional Voronoi cell.

Element formulation for elasticity and fracture simulations

A lattice element is defined by two neighbouring nodes, i and j, and their common Voronoi facet (Fig. 14c). The element stiffness relations are based on a zero-size spring set, located at the area centroid (point C) of the Voronoi facet, and connected to the element nodes via rigid-arm constraints. The spring set consists of three axial springs, oriented normal and tangential to the facet, and three rotational springs about the same local (n-s-t) axes. The stiffness coefficients of the axial springs are:

$$k_s = k_t = \alpha_1 k_n = \alpha_1 \alpha_2 E \frac{A_{ij}}{h_{ij}}, \tag{11}$$

where A_{ij} is the Voronoi facet area; h_{ij} is the distance between nodes i and j; α_1 and α_2 are parameters, set in conjunction with a uniaxial tension test simulation, to provide macroscopic representation of both elastic modulus E and Poisson ratio ν [66]. For the special case of $\alpha_1 = \alpha_2 = 1$, the lattice is elastically homogeneous, although the corresponding $\nu = 0$. The stiffness coefficients of the rotational springs are:

$$k_{\phi n} = E \frac{J_p}{h_{ij}}, \quad k_{\phi s} = E \frac{I_{11}}{h_{ij}}, \quad k_{\phi t} = E \frac{I_{22}}{h_{ij}}, \tag{12}$$

where J_p is the polar moment of inertia of the facet area, and I_{11} and I_{22} are the two principal moments of inertia of the facet area. Directions s and t are aligned with the facet principal axes. The spring constants appear on the diagonal of the material matrix, $\mathbf{D}$, given by

$$\mathbf{D} = (1 - \omega) \operatorname{diag} \left[k_n, \ k_s, \ k_t, \ k_{\phi n}, \ k_{\phi s}, \ k_{\phi t} \right], \tag{13}$$

where ω is a scalar damage parameter used to model material fracture, as described in Section 3.2. Prior to fracture initiation, $\omega = 0$.

The generalized spring displacements $\mathbf{d}$ (each corresponding to one of the six spring constants defined in Eqs. (11) and (12)) are related to the generalized nodal displacements in element local coordinates, $\mathbf{u_e}$, by

$$\mathbf{d} = \mathbf{B}\mathbf{u}_e, \tag{14}$$

where $\mathbf{B}$ and its submatrices have the following forms:

$$\mathbf{B} = \begin{bmatrix} -\mathbf{I} & \mathbf{B}_{12} & \mathbf{I} & \mathbf{B}_{14} \\ \mathbf{0} & -\mathbf{I} & \mathbf{0} & \mathbf{I} \end{bmatrix}, \tag{15a}$$

$$\mathbf{B}_{12} = \begin{bmatrix} 0 & -z_C & y_C \\ z_C & 0 & -h/2 \\ -y_C & h/2 & 0 \end{bmatrix}, \quad \mathbf{B}_{14} = \begin{bmatrix} 0 & z_C & -y_C \\ -z_C & 0 & -h/2 \\ y_C & -h/2 & 0 \end{bmatrix}. \tag{15b}$$

In Eq. (15), $\mathbf{I}$ is the identity matrix, and y_C and z_C are the offsets of the facet area centroid C from the y and z axes of the element, respectively (Fig. 14c). Using the principal of virtual work, the element stiffness matrix (with respect to element local coordinates) is

$$\mathbf{K}_e = \mathbf{B}^T \mathbf{D} \mathbf{B}. \tag{16}$$

After transforming $\mathbf{K}_e$ to global coordinates, the direct stiffness approach is used to assemble element stiffness matrices and internal force contributions into the structural equation set.
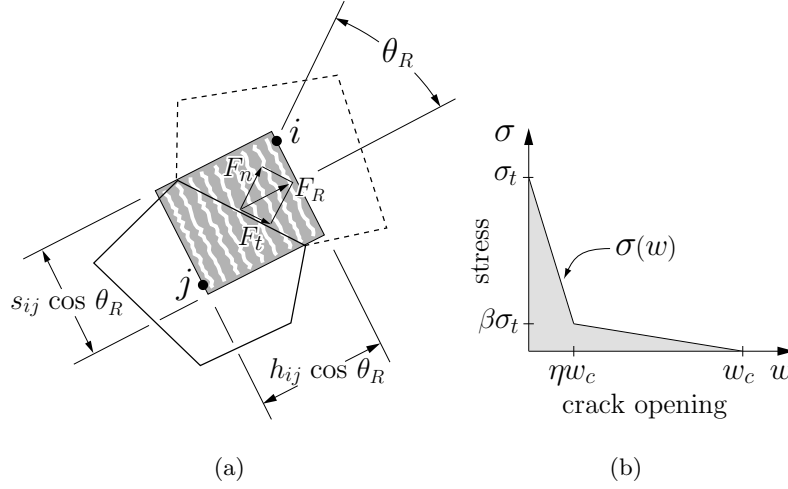
Fig. 16. (a) Crack band definition for planar analysis; and (b) material softening relation.

3.2 Crack band model of fracture

The modelling of fracture is based on the crack band concept of Bažant and Oh [3], which is easiest to visualize in two dimensions (Fig. 16a). Tensile loading of element ij will generally be skew to the element axis, so that both the normal and tangential springs are activated (with the normal spring in tension). The fracture criterion is based on the following measure of stress:

$$\sigma_R = \frac{F_R}{A_{ij}^P} \; , \tag{17}$$

where F_R is the resultant of the spring set forces and A_{ij}^P is the projection of the facet area on a plane perpendicular to the direction of F_R. For the two-dimensional case shown in Fig. 16a, $A_{ij}^P = s_{ij} \cos \theta_R t$, where t is the structural component thickness.

For each iteration of the solution process, the ratio $\sigma_R/\sigma(w)$ is determined for all of the lattice elements, where cohesive stress $\sigma(w)$ is a prescribed function of the crack opening displacement w. A bilinear function is assumed as shown in Fig. 16b, where σ_t is the uniaxial tensile strength of the material and w_c is the traction-free crack opening displacement; parameters β and η locate the break in slope in the bilinear softening diagram. A prismatic crack zone initiates (or continues to develop) within the element with $\max\left(\sigma_R/\sigma(w)\right) > 1$. The dimensions of crack zone conform to the local geometry of the Voronoi diagram (Fig. 16a). The solution procedure determines fracture strain ε_R in the direction of F_R, from which crack opening displacement is obtained:

$$w = \varepsilon_R \ h_{ij} \cos \theta_R. \tag{18}$$

As is customary for lattice models, the stiffness properties of (at most) one element are modified per computational cycle. Element fracture involves an isotropic reduction of the spring stiffnesses, by incrementing ω in Eq. (13), and an associated release of spring forces so that σ_R follows the bilinear softening relation. The range of the damage parameter is $0 \le \omega \le 1$, with $\omega = 1$ corresponding to the traction-free condition. This secant stiffness approach avoids negative stiffness terms and the numerical instabilities that can arise from their use. To reduce computational cost, a Cholesky factorization of the structural stiffness matrix is performed only once at the beginning of the analysis. Subsequent modifications of the element stiffness matrices (to account for fracture) are implemented at the system level through low-rank updating of the Cholesky factorization [65].

3.3 Fracture simulations

Basic capabilities of this irregular lattice model are illustrated in the following two examples. The first example demonstrates the ability to reproduce the prescribed softening behaviour without stress locking; the second example concerns the modelling of a series of concrete specimens under uniaxial tension.

Model tension test

For the model tension test shown in Fig. 17a, the stress σ_R is uniform throughout the lattice (and equals $\sigma = P/A$, where A is the model cross-section area). For increasing axial load, σ_R reaches the tensile strength σ_t in all elements simultaneously, so that a minute reduction of σ_t for any one element initiates fracture within that element. Continued loading leads to the formation of a traction-free crack through the entire cross-section (Fig. 17b). Model response at the structural scale (shown in Fig. 17c) corresponds precisely to the prescribed softening curve.

For the sake of illustration, consider the fracture criterion to be: `max` $(\sigma_n/\sigma(w)) > 1$, where $\sigma_n = F_n/A_{ij}$. For this case, the crack band is constrained to form normal to the element axis and at least two sources of error are present: 1) $\sigma_n < \sigma$, unless the element axis is aligned with the direction of tensile loading; and 2) after fracture initiation, the component of crack opening in the direction of the element axis is smaller than that in the direction of loading. These inaccuracies cause excess strength and energy consumption, as indicated by the broken line in Fig. 17c, which can be regarded as a form of stress locking. The amount of overstrength and excess energy consumption depends on the orientation of the elements crossing the fracture surface. Further discussion of this example is given in Reference [7].
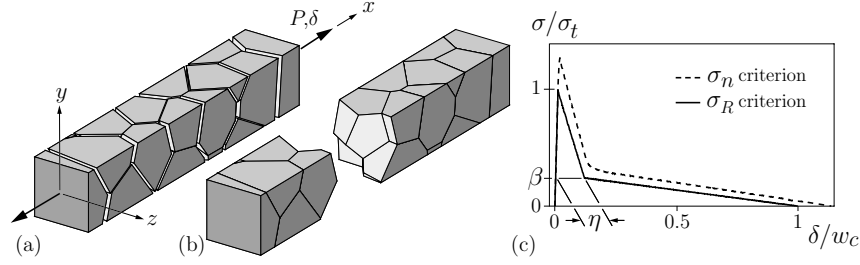
Fig. 17. Basic validation of fracture model (figure adapted from [7]).

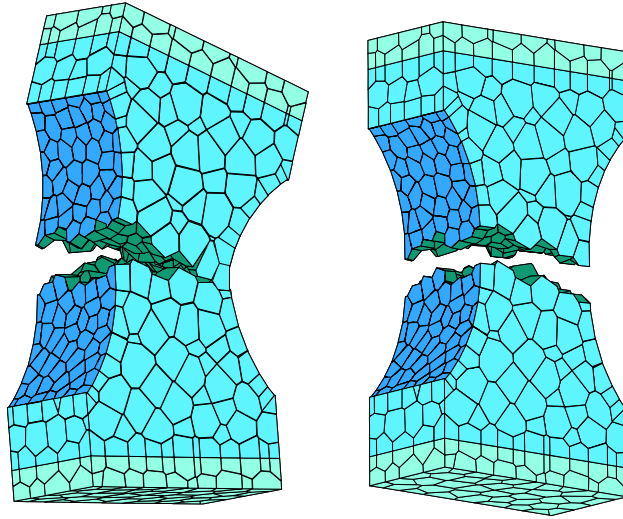## Uniaxial tension test simulation

The specimen dimensions and boundary conditions (shown as the insert in Fig. 18a) correspond to one of several series of geometrically similar specimens tested by van Vliet and van Mier [62]. The nominal size of the specimens is $D = 200$ mm and the thickness is 100 mm; the gage length over which displacements are measured is $0.6D$. The reported concrete properties, averaged over the seven specimens in the series, were used as input to the model: elastic modulus $E = 39.8$ GPa; tensile strength $\sigma_t = 2.75$ MPa; and specific fracture energy $G_F = 124$ N/m. The shape of the softening diagram was assumed to be bilinear with $\beta = 0.25$ and η set to provide the reported G_F value.

The lattice model results (for both the σ_R and σ_n fracture criteria) are compared with the experimental results in Fig. 18a. For the σ_R criterion, the numerical results run within the range of the experimental results and, for continued loading, approach the traction-free condition. After fracture localization on one side of the specimen, symmetry of the resisting section is lost, so that fracture is driven by both the uniaxial tensile load and local bending (Fig. 18b). For the case where rotation is prevented at the specimen ends, crack opening is more uniform over the cross-section (Fig. 18c), as was the case for the model tension test described earlier.

The total energy consumed by the fracture process is equal to the area under the load-displacement curve. Dividing total energy by the cracked liga-ment area yields the specific fracture energy, which is 132.3 N/m (or 1.071 G_F) for the σ_R criterion. The increase in energy consumption over the target G_F is due to the tendency of the incremental loading procedure to overshoot the fracture strength (i.e. $\sigma > \sigma_t$ for some elements). Smaller load steps and/or retracting the loads to precisely meet the σ_R criterion would improve agree-ment with the target G_F. On the other hand, when using the σ_n criterion, the average specific fracture energy obtained by simulation is 552.5 N/m (or 4.456G_F). The same form of stress locking of the σ_n approach was observed for two-dimensional analyses of crack propagation [10].
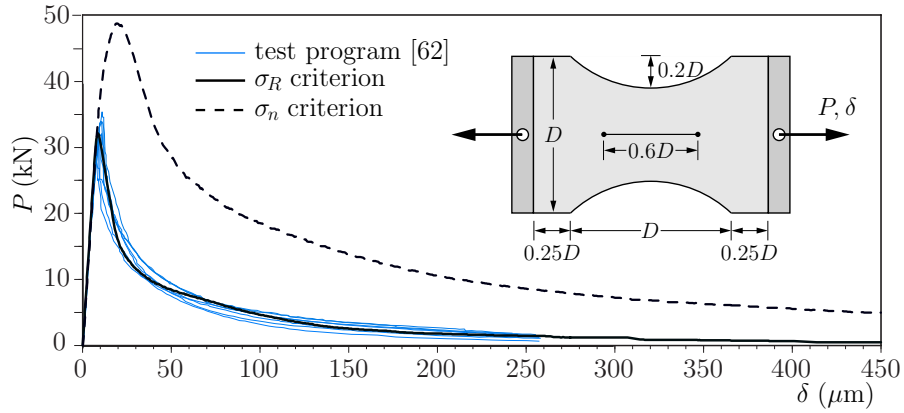
(a)

(b)   (c)

Fig. 18. Uniaxial tension test simulation. (a) load-displacement response; (b) simulated displacements allowing for support rotation (as per experiment); and (c) simulated displacements for fixed supports.

4 Concluding Remarks

This paper described recent research on the use of Voronoi-based interpolants and Voronoi grids in computer modelling and simulation of physical phe-

nomena. Emphasis was placed on two applications—development of polygonal finite elements for crack propagation simulations, and a Voronoi-based lattice model of cohesive cracking in quasi-brittle materials. The Laplace interpolant [12] was used to construct basis functions on convex polygons and quadtree meshes. The polygonal basis functions were used within the framework of partition of unity for crack growth simulations. Numerical examples were presented to demonstrate the versatility of this approach. In the lattice model, the Laplace weight, $\alpha_{ij} = s_{ij}/h_{ij}$, scales the local stiffness terms for the element connecting nodes i and j. Fracture was represented using a crack band approach, in which the dimensions of the crack band were also scaled according to the Voronoi diagram. This enabled grid insensitive, objective simulations of mode-I fracture to be realized on irregular lattice networks.

Finite elements—with their robustness, accuracy, and rigorous theoretical underpinnings—remain the most widely accepted choice for continuum fracture and crack propagation simulations. However, over the past decade, mesh-independent crack modeling using partition-of-unity enrichment techniques has become in many instances more versatile than traditional finite element methods for failure modeling. Unlike brittle materials where linear elastic fracture mechanics principles are applicable, modeling of quasi-brittle materials such as concrete poses many challenges in computational fracture [18]. The use of discrete (Voronoi) lattice models to describe fracture processes in multi-phase materials with distinct features (fibers, inclusions, secondary phases, etc.) is particularly promising. Significant research opportunities exist for advancing computational fracture modeling to effectively capture the transition from continua to discontinua at the meso-scale.

5 Acknowledgements

References

1. S. N. Atluri and S. Shen. *The Meshless Local Petrov-Galerkin (MLPG) Method*. Tech Science Press, Encino, CA, 2002.
2. I. Babuška and J. M. Melenk. Partition of unity method. *International Journal for Numerical Methods in Engineering*, 40:727–758, 1997.
3. Z. P. Bažant and B. H. Oh. Crack band theory for fracture of concrete. *Materials and Structures*, 16:155–176, 1983.
4. V. V. Belikov, V. D. Ivanov, V. K. Kontorovich, S. A. Korytnik, and A. Yu. Semenov. The non-Sibsonian interpolation: A new method of interpolation of the

values of a function on an arbitrary set of points. *Computational Mathematics and Mathematical Physics*, 37(1):9–15, 1997.

5. T. Belytschko and T. Black. Elastic crack growth in finite elements with minimal remeshing. *International Journal for Numerical Methods in Engineering*, 45:601–620, 1999.

6. T. Belytschko, Y. Krongauz, D. Organ, M. Fleming, and P. Krysl. Meshless methods: An overview and recent developments. *Computer Methods in Applied Mechanics and Engineering*, 139:3–47, 1996.

7. S. Berton and J. E. Bolander. Crack band modeling of fracture in irregular lattices. *Computer Methods in Applied Mechanics and Engineering*, 195:7172–7181, 2006.

8. J-D. Boissonnat and J. Flötotto. A coordinate system associated with points scattered on a surface. *Computer-Aided Design*, 36(2):161–174, 2004.

9. J. E. Bolander and S. Saito. Fracture analysis using spring networks with random geometry. *Engineering Fracture Mechanics*, 61:569–591, 1998.

10. J. E. Bolander and N. Sukumar. Irregular lattice model for quasistatic crack propagation. *Physical Review B*, 71:094106, 2005.

11. J. Braun and M. Sambridge. A numerical method for solving partial differential equations on highly irregular evolving grids. *Nature*, 376:655–660, 1995.

12. N. H. Christ, R. Friedberg, and T. D. Lee. Weights of links and plaquettes in a random lattice. *Nuclear Physics B*, 210(3):337–346, 1982.

13. E. Cueto, M. Doblaré, and L. Gracia. Imposing essential boundary conditions in the natural element method by means of density-scaled α-shapes. *International Journal for Numerical Methods in Engineering*, 49(4):519–546, 2000.

14. E. Cueto, N. Sukumar, B. Calvo, M. A. Martínez, J. Cegoñino, and M. Doblaré. Overview and recent advances in natural neighbour Galerkin methods. *Archives of Computational Methods in Engineering*, 10(4):307–384, 2003.

15. G. Cusatis, Z. P. Bažant, and L. Cedolin. Confinement-shear lattice model for concrete damage in tension and compression: I. Theory. *Journal of Engineering Mechanics*, 129:1439–1448, 2003.

16. G. Cusatis, Z. P. Bažant, and L. Cedolin. Confinement-shear lattice csl model for fracture propagation in concrete. *Computer Methods in Applied Mechanics and Engineering*, 195(52):7154–7171, 2006.

17. G. Dasgupta. Interpolants within convex polygons: Wachspress' shape functions. *Journal of Aerospace Engineering*, 16(1):1–8, 2003.

18. R. de Borst, J. J. C. Remmers, A. Needleman, and M.-A. Abellan. Discrete vs smeared crack models for concrete fracture: bridging the gap. *International Journal for Numerical and Analytical Methods in Geomechanics*, 28(7–8):583–607, 2004.

19. H. Edelsbrunner, D. G. Kirkpatrick, and R. Seidel. On the shape of a set of points in the plane. *IEEE Transactions on Information Theory*, IT-29(4):551–559, 1983.

20. H. Edelsbrunner and E. Mcke. Three dimensional alpha shapes. *ACM Transactions on Graphics*, 13:43–72, 1994.

21. G. Farin. Surfaces over Dirichlet tessellations. *Computer Aided Geometric Design*, 7(1–4):281–292, 1990.

22. M. S. Floater. Mean value coordinates. *Computer Aided Geometric Design*, 20(1):19–27, 2003.

23. M. S. Floater, G. Kós, and M. Reimers. Mean value coordinates in 3D. *Computer Aided Geometric Design*, 22(7):623–631, 2005.

24. T. P. Fries and H. G. Matthies. Classification and overview of meshfree methods. Technical Report Informatikbericht-Nr. 2003-03, Institute of Scientific Computing, Technical University Braunschweig, Braunschweig, Germany, 2004.

25. H. J. Herrmann, A. Hansen, and S. Roux. Fracture of disordered, elastic lattices in two dimensions. *Physical Review B*, 39(1):637, 1989.

26. H. J. Herrmann and S. Roux, editors. *Statistical Models for the Fracture of Disordered Media*. North-Holland, Amsterdam, The Netherlands, 1990.

27. H. Hiyoshi and K. Sugihara. Two generalizations of an interpolant based on Voronoi diagrams. *International Journal of Shape Modeling*, 5(2):219–231, 1999.

28. H. Hiyoshi and K. Sugihara. Improving continuity of Voronoi-based interpolation over Delaunay spheres. *Computational Geometry*, 22:167–183, 2002.

29. K. Hormann and M. S. Floater. Mean value coordinates for arbitrary planar polygons. *ACM Transaction on Graphics*, 25(4):1424–1421, 2006.

30. R. Huang, N. Sukumar, and J.-H. Prévost. Modeling quasi-static crack growth with the extended finite element method. part II: Numerical applications. *International Journal of Solids and Structures*, 40(26):7539–7552, 2003.

31. S. R. Idelsohn, N. Calvo, and E. Onate. Polyhedralization of an arbitrary 3D point set. *Computer Methods in Applied Mechanics and Engineering*, 192(22–24):2649–2667, 2003.

32. S. R. Idelsohn, E. Onate, N. Calvo, and F. Del Pin. Meshless finite element method. *International Journal for Numerical Methods in Engineering*, 58(6):893–912, 2003.

33. P. Kagan, A. Fischer, and P. Z. Bar-Yoseph. Mechanically based models: Adaptive refinement for B-spline finite element. *International Journal for Numerical Methods in Engineering*, 57(8):1145–1175, 2003.

34. P. Krysl, A. Trivedi, and B. Zhu. Object-oriented hierarchical mesh refinement with CHARMS. *International Journal for Numerical Methods in Engineering*, 60(8):1401–1424, 2004.

35. J. J. Laguardia, E. Cueto, and M. Doblaré. A natural neighbour Galerkin method with quadtree structure. *International Journal for Numerical Methods in Engineering*, 63:789–812, 2005.

36. S. Li and W. K. Liu. *Meshfree Particle Methods*. Springer-Verlag, New York, NY, 2004.

37. G. R. Liu. *Mesh Free Methods: Moving Beyond the Finite Element Method*. CRC Press, Boca Raton, FL, 2003.

38. E. A. Malsch and G. Dasgupta. Shape functions for polygonal domains with interior nodes. *International Journal for Numerical Methods in Engineering*, 61(12):1153–1172, 2004.

39. E. A. Malsch, J. J. Lin, and G. Dasgupta. Smooth two dimensional interpolants: a recipe for all polygons. *Journal of Graphics Tools*, 10(2):11–23, 2005.

40. M. Meyer, H. Lee, A. Barr, and M. Desbrun. Generalized barycentric coordinates on irregular polygons. *Journal of Graphics Tools*, 7(1):13–22, 2002.

41. I. D. Mishev. Finite volume methods on Voronoi meshes. *Numerical Methods for Partial Differential Equations*, 14:193–212, 1998.

42. N. Moës, J. Dolbow, and T. Belytschko. A finite element method for crack growth without remeshing. *International Journal for Numerical Methods in Engineering*, 46(1):131–150, 1999.

43. A. Okabe, B. Boots, and K. Sugihara. *Spatial Tessellations: Concepts and Applications of Voronoi Diagrams*. John Wiley & Sons, Chichester, England, 1992.

44. U. Pinkall and K. Polthier. Computing discrete minimal surfaces and their conjugates. *Experimental Mathematics*, 2(1):15–36, 1993.

45. H. Samet. The quadtree and related hierarchical data structure. *ACM Computing Surveys*, 16(2):187–260, 1984.

46. E. Schlangen and E. J. Garboczi. New method for simulating fracture using an elastically uniform random geometry. *International Journal of Engineering Science*, 34(10):1131–1144, 1996.

47. E. Schlangen and J. G. M. van Mier. Experimental and numerical analysis of micromechanisms of fracture of cement-based composites. *Cement and Concrete Composites*, 14:105–118, 1992.

48. R. Sibson. A vector identity for the Dirichlet tesselation. *Mathematical Proceedings of the Cambridge Philosophical Society*, 87:151–155, 1980.

49. N. Sukumar. *The Natural Element Method in Solid Mechanics*. Ph.D. thesis, Theoretical and Applied Mechanics, Northwestern University, Evanston, IL, U.S.A., June 1998.

50. N. Sukumar. Voronoi cell finite difference method for the diffusion operator on arbitrary unstructured grids. *International Journal for Numerical Methods in Engineering*, 57(1):1–34, 2003.

51. N. Sukumar. Construction of polygonal interpolants: A maximum entropy approach. *International Journal for Numerical Methods in Engineering*, 61:2159–2181, 2004.

52. N. Sukumar and E. A. Malsch. Recent advances in the construction of polygonal finite element interpolants. *Archives of Computational Methods in Engineering*, 13(1):129–163, 2006.

53. N. Sukumar and B. Moran. C^1 natural neighbor interpolant for partial differential equations. *International Journal for Numerical Methods in Engineering*, 15(4):417–447, 1999.

54. N. Sukumar, B. Moran, and T. Belytschko. The natural element method in solid mechanics. *International Journal for Numerical Methods in Engineering*, 43(5):839–887, 1998.

55. N. Sukumar, B. Moran, A. Yu Semenov, and V. V. Belikov. Natural neighbor Galerkin methods. *International Journal for Numerical Methods in Engineering*, 50(1):1–27, 2001.

56. N. Sukumar and A. Tabarraei. Conforming polygonal finite elements. *International Journal for Numerical Methods in Engineering*, 61(12):2045–2066, 2004.

57. N. Sukumar and R. W. Wright. Overview and construction of meshfree basis functions: From moving least squares to entropy approximants. *International Journal for Numerical Methods in Engineering*, 70(2):181–205, 2007.

58. A. Tabarraei and N. Sukumar. Adaptive computations on conforming quadtree meshes. *Finite Elements in Analysis and Design*, 41(7–8):686–702, 2005.

59. A. Tabarraei and N. Sukumar. Adaptive computations using material forces and residual-based error estimators on quadtree meshes. *Computer Methods in Applied Mechanics and Engineering*, 196(25–28):2657–2680, 2007.

60. A. Tabarraei and N. Sukumar. Extended finite element method on polygonal and quadtree meshes. *Computer Methods in Applied Mechanics and Engineering*, 197(5):425–438, 2008.

61. J. G. M. van Mier. Multi-scale interaction potentials $(f - r)$ for describing fracture of brittle disordered materials like cement and concrete. *International Journal of Fracture*, 143, 2007.

62. M. R. A. van Vliet and J. G. M. van Mier. Effect of strain gradients on the size effect of concrete in uniaxial tension. *International Journal of Fracture*, 95:195–219, 1999.
63. E. L. Wachspress. *A Rational Finite Element Basis*. Academic Press, N. Y., 1975.
64. B. Widom. Random sequential addition of hard spheres to a volume. *Journal of Chemical Physics*, 44:3888–3894, 196.
65. M. Yip, Z. Li, B.-S. Liao, and J. E. Bolander. Irregular lattice models of fracture of multiphase particulate materials. *International Journal of Fracture*, 140(1–4):113–124, 2006.
66. M. Yip, J. Mohle, and J. E. Bolander. Automated modeling of 3-d structural components using irregular lattices. *Journal of Computed-Aided Civil and Infrastructure Engineering*, 20(6):393–407, 2005.